

Manuscript version: Author's Accepted Manuscript

The version presented in WRAP is the author's accepted manuscript and may differ from the published version or Version of Record.

Persistent WRAP URL:

<http://wrap.warwick.ac.uk/159876>

How to cite:

Please refer to published version for the most recent bibliographic citation information.

Copyright and reuse:

The Warwick Research Archive Portal (WRAP) makes this work by researchers of the University of Warwick available open access under the following conditions.

Copyright © and all moral rights to the version of the paper presented here belong to the individual author(s) and/or other copyright owners. To the extent reasonable and practicable the material made available in WRAP has been checked for eligibility before being made available.

Copies of full items can be used for personal research or study, educational, or not-for-profit purposes without prior permission or charge. Provided that the authors, title and full bibliographic details are credited, a hyperlink and/or URL is given for the original metadata page and the content is not changed in any way.

Publisher's statement:

Please refer to the repository item page, publisher's statement section, for further information.

For more information, please contact the WRAP Team at: wrap@warwick.ac.uk.

1 **CO gas produced by a giant impact in the inner region of a** 2 **young system**

3
4 Tajana Schneiderman^{1*}, Luca Matr ², Alan P. Jackson^{3,4}, Grant M. Kennedy^{5,6}, Quentin Kral⁷,
5 Sebasti n Marino⁸, Karin I.  berg⁹, Kate Y. L. Su¹⁰, David J. Wilner⁹, Mark C. Wyatt⁸

6
7 **Models of terrestrial planet formation predict that the final stages of planetary assembly,**
8 **lasting tens of millions of years beyond the dispersal of young protoplanetary disks, are**
9 **dominated by planetary collisions. It is through these giant impacts that planets like the**
10 **young Earth grow to their final mass and achieve long-term stable orbital**
11 **configurations¹. A key prediction is that these impacts produce debris. To date, the most**
12 **compelling observational evidence for post-impact debris comes from the planetary**
13 **system around the nearby 23 Myr-old A star HD 172555. This system shows large**
14 **amounts of fine dust with an unusually steep size distribution and atypical dust**
15 **composition, previously attributed to either a hypervelocity impact^{2,3} or a massive**
16 **asteroid belt⁴. Here, we report the spectrally resolved detection of a CO gas ring co-**
17 **orbiting with dusty debris between ~6-9 au - a region analogous to the outer terrestrial**
18 **planet region of our Solar System. Taken together, the dust and CO detections favor a**

¹ Department of Earth, Atmospheric and Planetary Sciences, Massachusetts Institute of Technology, Cambridge, Massachusetts, USA

² Centre for Astronomy, School of Physics, National University of Ireland Galway, University Road, Galway, Ireland

³ Centre for Planetary Sciences, University of Toronto at Scarborough, 1265 Military Trail, Toronto, ON M1C 1A4, Canada

⁴ School of Earth and Space Exploration, Arizona State University, 781 E. Terrace Mall, Tempe, AZ 85287, USA

⁵ Department of Physics, University of Warwick, Coventry CV4 7AL, UK

⁶ Centre for Exoplanets and Habitability, University of Warwick, Gibbet Hill Road, Coventry CV4 7AL, UK

⁷ LESIA, Observatoire de Paris, Universit  PSL, CNRS, Sorbonne Universit , Univ. Paris Diderot, Sorbonne Paris Cit , 5 place Jules Janssen, F-92195 Meudon, France

⁸ Institute of Astronomy, University of Cambridge, Madingley Road, Cambridge CB3 0HA, UK

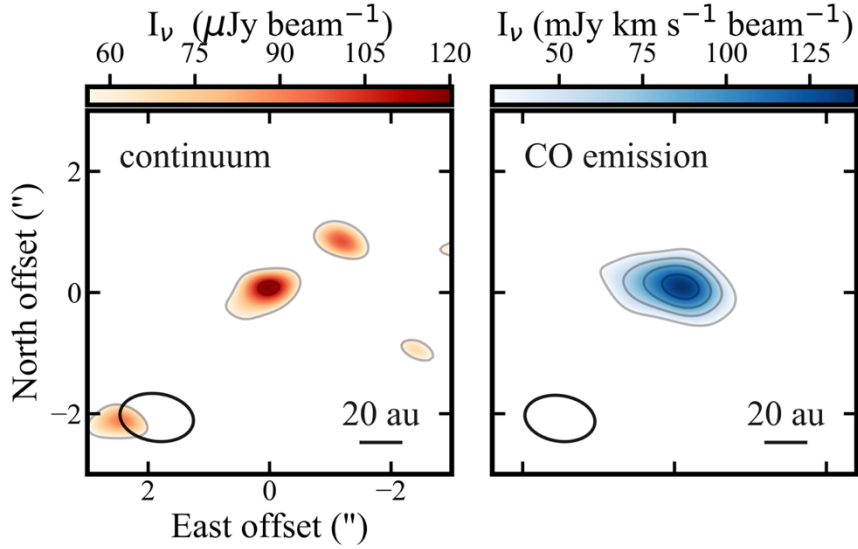
⁹ Center for Astrophysics | Harvard & Smithsonian, 60 Garden Street, Cambridge, MA 02138, USA

¹⁰ Steward Observatory, University of Arizona, 933 N. Cherry Avenue, Tucson, AZ 85721, USA

19 **giant impact between large, volatile-rich bodies. This suggests that planetary-scale**
20 **collisions, analogous to the Moon-forming impact, can release large amounts of gas as**
21 **well as debris, and that this gas is observable, providing a window into the composition**
22 **of young planets.**

23 HD 172555 is a 23 ± 3 Myr-old⁵ A type star with a mass of $1.76 M_{\odot}$ ⁶ and luminosity of
24 $7.7 L_{\odot}$, located 28.5 pc ^{7,8} from Earth within the young β Pictoris moving group⁹. Its planetary
25 system hosts large amounts of dust in the terrestrial region, producing an infrared (IR) excess
26 best fit by warm (290 K) dust¹⁰ with an infrared luminosity 7.2×10^{-4} times that of its host star⁴.
27 Spatially resolved mid-IR observations constrain this dust to a disk of material in the inner,
28 $<10 \text{ au}$ region, viewed close to edge-on from Earth^{11,12}. Rare solid-state emission features
29 detected at $8\text{-}9.3\mu\text{m}$ ¹³ indicate the presence of glassy silica (tektites and obsidian) and solid
30 SiO. These require high temperature processing and vapor condensation, supporting a
31 hypervelocity ($>10 \text{ km/s}$) impact between planetary bodies for the origin of the dust^{2,3}.
32 Detailed, self-consistent modelling indicates that this impact scenario can explain the spectral
33 features, as well as the overabundance of sub- μm sized grains and steep size distribution
34 inferred from the *Spitzer* IR spectrum³.

35 We used the Atacama Large Millimeter/submillimeter Array (ALMA) to detect dust
36 continuum and CO J=2-1 gas emission from the HD 172555 system (Fig. 1). The compact,
37 spatially unresolved dust and gas emission originates from within 15 au of the star, consistent
38 with previous IR and optical observations. The spectrum of CO in Fig. 2a is extracted from the
39 ALMA data cube and is spectrally resolved. The double-peaked profile is expected from gas
40 orbiting in Keplerian rotation around the central star. The centroid of the CO profile is at a
41 heliocentric velocity of $2.3\pm 0.2 \text{ km/s}$, consistent with the stellar velocity¹⁴, confirming that the
42 gas emission is associated with the HD 172555 system.



43

44 **Figure 1** | Cleaned emission maps of the HD 172555 system. Left panel is a $\sim 4\sigma$ detection of the dust continuum
 45 emission. Right panel is the moment-0 CO J=2-1 transition, with a $\sim 9\sigma$ detection. Contour levels are at 2σ
 46 intervals, with σ being $0.029 \text{ mJy beam}^{-1}$ and $15 \text{ mJy km s}^{-1} \text{ beam}^{-1}$ for the continuum and CO moment-0 maps,
 47 respectively. Beam size denoted in lower left corner of each panel. Note that the 2σ peaks are background noise
 48 and not significant.

49

50

51

52

53

54

55

56

57

58

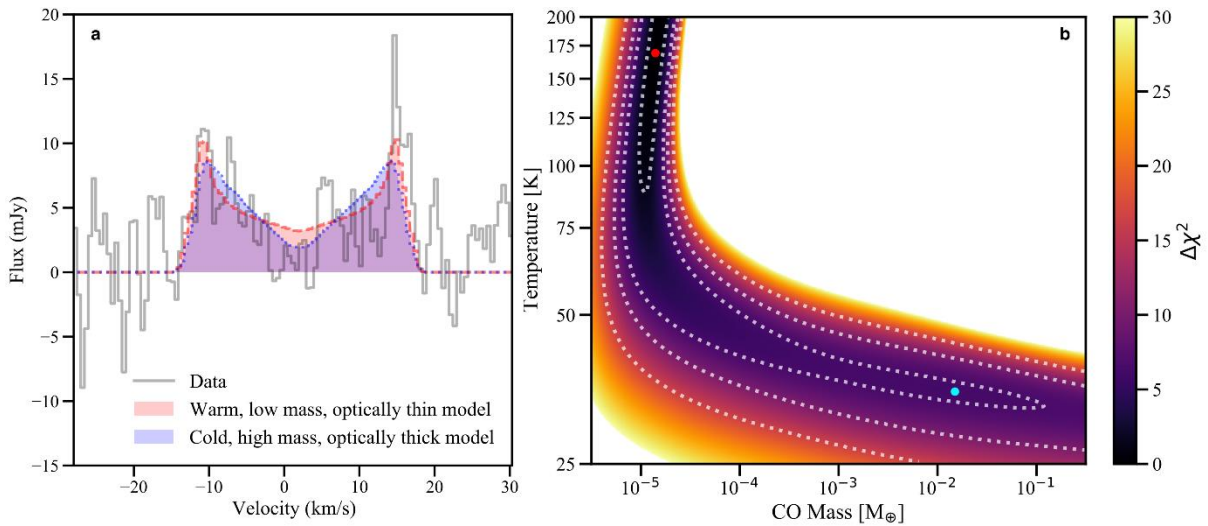
59

60

We modelled the CO emission as a vertically thin ring of optically thin gas with radially and azimuthally uniform surface density between an inner and outer boundary, in Keplerian rotation around the central star. We find that the CO is confined to a ring of radius $\sim 7.5 \text{ au}$ and width $\sim 3.3 \text{ au}$. The data are consistent with a symmetric disk model; we find no strong evidence of asymmetry between the blue- and red-shifted sides of the CO spectral line profile. We convert the integrated flux of 120 mJy km/s to a CO gas mass considering non-local thermodynamic equilibrium excitation, finding masses in the range between $(0.45\text{-}1.21) \times 10^5 M_{\oplus}$ for temperatures between 100 and 250 K. The total millimetre dust mass, as calculated from the observed continuum emission, is $(1.8 \pm 0.6) \times 10^{-4} M_{\oplus}$ for an expected equilibrium blackbody temperature of 169 K at 7.5 au.

To test our assumption that the CO J=2-1 emission is optically thin, we create a full 3D radiative transfer model of the ring with the spatial morphology described above. For a gas

61 temperature comparable to, or higher than the expected blackbody temperature of 169 K at 7.5
 62 au, we find low optical depths, which validates our optically thin assumption. This corresponds
 63 to total CO masses of $(1.4 \pm 0.3) \times 10^{-5} M_{\oplus}$ at 169 K. On the other hand, we find that colder
 64 ($\ll 100$ K) temperatures would require higher optical depth, and much higher CO masses to
 65 reproduce our observed CO line emission (Fig. 2b). This temperature-mass degeneracy can be
 66 resolved by the detailed spectral shape of the emission since models of optically thin, warm
 67 gas constrained to a narrow ring produce sharper peaks compared to the optically thick, cold
 68 models (Fig. 2a). We find that the data prefer less massive, warmer models (lower χ^2).



69
 70 **Figure 2** | Mass-temperature degeneracy of the CO data. **a.** CO J=2-1 spectrum of HD172555 (grey solid line),
 71 compared to the output of two radiative transfer models: a low mass, warm temperature CO model (red dashed
 72 line), and a high mass, cold temperature CO model (blue dotted line). **b.** χ^2 map (where the χ^2 is relative to the
 73 best-fit model) showing a clear CO temperature-mass degeneracy for models that are good fits to the data (darker
 74 on the colour scale). The red and light blue dots correspond to the red (warm) and blue (cold) CO models shown
 75 in panel a. Dotted contours enclose models that are consistent with the data at the $>[1,2,3,4]$ σ confidence level.

76 The observed CO gas in the circumstellar environment around HD 172555 will be
 77 subject to photodissociation from the stellar and interstellar UV field. The former dominates at
 78 the 7.5 au location of the CO ring and causes CO (if unshielded) to be rapidly destroyed on a
 79 timescale of ~ 1 day. However, the lifetime of CO is extended when taking into account

80 shielding effects from atomic carbon¹⁵ (C, as produced by CO photodissociation), molecular
81 hydrogen (H₂), and CO itself (self-shielding), that prevent UV photons from penetrating into
82 the ring. Self-shielding alone, in the warm temperature, low CO mass scenario, extends the gas
83 lifetime by ~2-4 years. Given the lack of observational constraints on C and H₂ column
84 densities, we cannot definitively estimate the shielding and hence the CO destruction timescale.
85 However, CO could have easily survived over the system age (23 Myr) both in a scenario where
86 C and CO dominate the gas mass (C/CO ratio of > 0.16-0.43, see Methods), and in an H₂-
87 dominated scenario (H₂/CO > ~10⁵). Therefore, CO could either be the result of a very recent
88 production and/or replenishment mechanism, or have survived for a large fraction of the system
89 age.

90 The CO detection constrains the gas to be located in the ~6-9 au region of the
91 HD172555 planetary system, co-located with the dust¹². Accounting for the difference in
92 luminosity between the Sun and HD172555, this region corresponds to the same thermal
93 conditions as ~2.1-3.3 au - the Asteroid belt region - in our Solar System. This makes the
94 presence of CO, a highly volatile gas with sublimation temperatures as low as ~20 K, extremely
95 surprising in a system with age 23 Myr. Some physical mechanism must explain the presence
96 of gas and dust in the outer terrestrial planet forming region of HD 172555. We test four
97 hypotheses for the origin of the debris, and examine them in light of existing evidence from
98 both dust observations and from the ALMA detection of CO in the system. These scenarios
99 are: (i) leftover gas and dust from a primordial, protoplanetary disk, (ii) collisional production
100 within an extrasolar asteroid belt, (iii) inward transport of material from an external reservoir,
101 and (iv) release in the aftermath of a giant impact between planetary-sized bodies.

102 Young A-type stars are born surrounded by protoplanetary disks of primordial gas and
103 dust, but only ~2-3% survive beyond the first 3 Myr of a star's lifetime^{16,17}. Even if the CO
104 observed around HD 172555 were primordial, with its lifetime extended through shielding, the

105 system would remain a remarkable outlier not only in age (at 23 Myr old), but also in dust mass
106 (orders of magnitude lower than protoplanetary disks¹⁸) and in radial distribution of CO and
107 dust (constrained within 10 au, and with a CO cavity, in contrast to protoplanetary disks
108 typically extending out to tens/hundreds of au^{19,20}). The extreme depletion in dust mass would
109 require efficient dust removal, either through accretion onto the star or grain growth¹⁸. At the
110 same time, the confined radial extent would require interior/exterior truncation, for example by
111 as-yet undiscovered companions. Finally, HD172555's peculiar dust mineralogy (requiring
112 energetic processing) is seldom seen in young protoplanetary disks, although it may have arisen
113 in nebular shocks analogous to those that could have led to chondrule formation in the Solar
114 System²¹. In conclusion, a primordial scenario would make HD172555 an extreme outlier
115 amongst other protoplanetary disks, favouring instead second-generation production.

116 In the second-generation case, a steady-state collisional cascade within an asteroid belt
117 can explain the dust mass detected in the system²², but not its abnormally steep particle size
118 distribution³, or its mineralogy requiring high-energy collisions at velocities higher than
119 expected within typical belts^{2,3,13}. While CO gas is commonly observed within collisional
120 cascades in colder extrasolar Kuiper belt analogs at tens of au²³, there its presence can be
121 explained by release of CO gas initially trapped within icy bodies, or by desorption of CO₂ ice
122 followed by rapid photodissociation of CO₂ gas²⁴⁻²⁸. This picture is not plausible at 7.5 au;
123 studies of ice-bearing asteroids in the Solar System show that while retaining water ice in the
124 deep subsurface is possible, explaining the presence of outgassing main-belt comets in the
125 Asteroid belt, CO and CO₂ cannot remain trapped at these temperatures^{29,30}. Additionally, any
126 bodies forming at this location would be too warm to have formed with a significant reservoir
127 of CO or CO₂.

128 Alternatively, the observed dust and CO might originate from inward scattering of small
129 bodies (*exocomets*) from an outer, cold reservoir akin to the Solar System's Edgeworth-Kuiper

130 belt³¹. We first explore the possibility of gas and dust production through sublimation of Solar
131 System -like, 10-km sized exocomets. We find that this scenario can only reproduce the
132 observations if exocomets can be delivered on low eccentricity orbits, finding that the
133 exocomet replenishment rate could potentially be reconciled with the non-detection of an outer
134 belt (see Methods). However, this scenario cannot explain the relatively narrow radial
135 distribution of the CO ring, or the mineralogy of the observed dust, and is thus not likely. On
136 the other hand, it is possible that a single, cold, massive icy body is scattered inwards from an
137 undetected outer belt. To produce the observed, largely axisymmetric distribution of material
138 and dust mineralogy, the icy body would need to undergo a giant impact and release its CO or
139 CO₂ content. Assuming a 25% CO+CO₂ ice mass fraction, and complete ice release at impact,
140 we find that a dwarf planet (at least half the size of Pluto) would be needed to produce the
141 (lower limit on the) CO gas mass observed.

142 Finally, CO gas and dust could be produced by a giant impact between planetary bodies
143 formed in situ at ~7.5 au. The epoch of terrestrial planet formation, lasting from ~10-100 Myr,
144 is expected to be dominated by giant impacts. Within the solar system, there is abundant
145 evidence for the occurrence of giant impacts; the iron enrichment of Mercury^{32,33}, the formation
146 of the Moon³⁴⁻³⁶, the Martian hemispheric dichotomy^{37,38}, and the retrograde rotation of
147 Venus³⁹ are all hypothesized to have their origins in giant impacts. The HD 172555 system, at
148 23 Myr, is at the expected age that terrestrial planet formation proceeds through giant impacts;
149 the dust and gas observed in the system are located in a region that is analogous to the terrestrial
150 zone in our own solar system. Studies of post-impact dynamics allow us to set constraints on
151 progenitor masses and time since impact to be placed by considering the current spatial
152 distribution and mass of dust (see Methods). The dust in the system is axisymmetric within
153 observational uncertainties, implying that the time since impact is at least the debris
154 symmetrization timescale, which at 7.5 au is of order ~0.2 Myr⁴⁰. The width of the dust debris,

155 as resolved at shorter wavelengths^{11,12,i}, suggests a progenitor mass of order $\sim 8 M_{\oplus}$, though
156 the exact value is dependent on the radial width of the dust debris, see Methods. Impacts
157 between such bodies produce debris that would survive encounters with leftover planets, on a
158 timescale longer than symmetrization; this indicates that impacts of such planets could be
159 responsible for the observed, long-lived debris field.

160 Further supporting this scenario, we find that the optically thin CO gas mass detected
161 in the system $((0.45-1.21) \times 10^{-5} M_{\oplus})$, or ~ 10 times the mass of Earth's atmosphere, is
162 consistent with post-impact release from a planetary atmosphere. We note that any CO₂ in a
163 planetary atmosphere will rapidly be converted into observable CO if liberated from the
164 atmosphere, as CO₂ cannot be significantly shielded by C in the same way as CO because its
165 photodissociation bands extend further toward the optical⁴¹. Simulations show that up to 60%
166 of a modestly-sized, heavy atmosphere can be stripped in the initial shock of an impact^{42,43}.
167 We find that the observed CO mass, as well as the C needed to shield the CO for at least the
168 symmetrization timescale, require the release of an amount of CO₂ corresponding to just 9-23%
169 of the total present in the Venusian atmosphere⁴⁴. More (less) massive planets with similar
170 heavy atmospheres would require a smaller (larger) fraction of the atmosphere removed, or a
171 smaller (larger) abundance of CO and/or CO₂. For lighter, H₂-dominated atmospheres, longer-
172 term thermal effects can result in the stripping of the entire atmospheric envelope⁴⁵, in which
173 case once again an amount of CO and/or CO₂ consistent with the observations could plausibly
174 be liberated.

175 The detection and morphology of CO gas, combined with previous evidence from dust
176 imaging and spectroscopy, supports a picture where a giant impact took place at least 0.2 Myr
177 ago in the outer terrestrial planet forming region of the 23 Myr-old HD 172555 system.
178 Planetary-scale impacts are predicted to be commonplace in the latest stages of planet
179 formation; the discovery of CO gas in the terrestrial planet forming region, in amounts

180 consistent with the expectation from atmospheric stripping, suggests that giant impacts may
181 not only release copious, observable dust, but also detectable amounts of gas. Furthermore, this
182 discovery reveals the importance of gas release in post-impact dynamics, and highlights the
183 potential of using gas as a tool to search for giant impacts in nearby planetary systems, while
184 providing a unique window into the composition of young planets and their atmospheres.

- 185 1. Morbidelli, A., Lunine, J. ~I., O'Brien, D. ~P., Raymond, S. ~N. & Walsh, K. ~J. Building Terrestrial
186 Planets. *Annu. Rev. Earth Planet. Sci.* **40**, 251–275 (2012).
- 187 2. Lisse, C. M. *et al.* Abundant circumstellar silica dust and sio gas created by a giant hypervelocity
188 collision in the 12 myr hd172555 system. *Astrophys. J.* **701**, 2019–2032 (2009).
- 189 3. Johnson, B. C. *et al.* A self-consistent model of the circumstellar debris created by a giant hypervelocity
190 impact in the HD 172555 system. *Astrophys. J.* **761**, (2012).
- 191 4. Wyatt, M. C. *et al.* Steady State Evolution of Debris Disks around A Stars. *Astrophys. J.* **663**, 365–382
192 (2007).
- 193 5. Mamajek, E. E. & Bell, C. P. M. On the age of the β pictoris moving group. *Mon. Not. R. Astron. Soc.*
194 **445**, 2169–2180 (2014).
- 195 6. David, T. J. & Hillenbrand, L. A. The ages of early-type stars: Strömgren photometric methods
196 calibrated, validated, tested, and applied to hosts and prospective hosts of directly imaged exoplanets.
197 *Astrophys. J.* **804**, 146 (2015).
- 198 7. Prusti, T. *et al.* The Gaia mission. *Astron. Astrophys.* **595**, A1 (2016).
- 199 8. Brown, A. G. A. *et al.* Gaia Data Release 2: Summary of the contents and survey properties. *arXiv* **616**,
200 A1 (2018).
- 201 9. Zuckerman, B., Song, I., Bessell, M. S. & Webb, R. A. The β Pictoris Moving Group. *Astrophys. J.* **562**,
202 L87–L90 (2001).
- 203 10. Cote, J. B and A type stars with unexpectedly large colour excesses at IRAS wavelengths. *Astron.*
204 *Astrophys.* **181**, 77–84 (1987).
- 205 11. Smith, R., Wyatt, M. C. & Haniff, C. A. Resolving the terrestrial planet forming regions of HD113766
206 and HD172555 with MIDI. *Mon. Not. R. Astron. Soc.* **422**, 2560–2580 (2012).
- 207 12. Engler, N., Schmid, H. M., Quanz, S. P., Avenhaus, H. & Bazzon, A. Detection of scattered light from
208 the hot dust in HD 172555. *arXiv* **618**, 1–15 (2018).
- 209 13. Chen, C. H. *et al.* Spitzer IRS Spectroscopy of IRAS -discovered Debris Disks . *Astrophys. J. Suppl.*
210 *Ser.* **166**, 351–377 (2006).
- 211 14. Gontcharov, G. A. Pulkovo Compilation of Radial Velocities for 35 495 Hipparcos stars in a common
212 system. *Astron. Lett.* **32**, 759–771 (2006).
- 213 15. Kral, Q., Marino, S., Wyatt, M. C., Kama, M. & Matrà, L. Imaging [CI] around HD 131835:
214 reinterpreting young debris discs with protoplanetary disc levels of CO gas as shielded secondary discs.
215 *\mnras* **489**, 3670–3691 (2019).
- 216 16. Kennedy, G. M. & Kenyon, S. J. Stellar mass dependent disk dispersal. *Astrophys. J.* **695**, 1210–1226
217 (2009).
- 218 17. Ribas, Á., Bouy, H. & Merín, B. Protoplanetary disk lifetimes vs. stellar mass and possible implications
219 for giant planet populations. *Astron. Astrophys.* **576**, A52 (2015).
- 220 18. Wyatt, M. C., Panić, O., Kennedy, G. M. & Matrà, L. Five steps in the evolution from protoplanetary to
221 debris disk. *Astrophys. Space Sci.* **357**, 103 (2015).
- 222 19. Isella, A. *et al.* The Disk Substructures at High Angular Resolution Project (DSHARP) - IX: A high
223 definition study of the HD 163296 planet forming disk. *arXiv* **869**, L49 (2018).
- 224 20. Boehler, Y. *et al.* The complex morphology of the young disk MWC 758: Spirals and dust clumps
225 around a large cavity. *arXiv* **853**, 162 (2017).
- 226 21. Morris, M. A. & Desch, S. J. Thermal histories of chondrules in solar nebula shocks. *Astrophys. J.* **722**,
227 1474–1494 (2010).
- 228 22. Su, K. Y. L. *et al.* Mid-infrared Studies of HD 113766 and HD 172555: Assessing Variability in the
229 Terrestrial Zone of Young Exoplanetary Systems. *arXiv* **898**, 21 (2020).
- 230 23. Matrà, L., Öberg, K. I., Wilner, D. J., Olofsson, J. & Bayo, A. On the ubiquity and stellar luminosity
231 dependence of exocometary CO gas: Detection around M dwarf TWA 7. *arXiv* **157**, 117 (2019).
- 232 24. Matrà, L., Panić, O., Wyatt, M. C. & Dent, W. R. F. CO mass upper limits in the Fomalhaut ring - The
233 importance of NLTE excitation in debris discs and future prospects with ALMA. *Mon. Not. R. Astron.*
234 *Soc.* **447**, 3936–3947 (2015).
- 235 25. Marino, S. *et al.* Exocometary gas in the HD 181327 debris ring. *Mon. Not. R. Astron. Soc.* **460**, 2933–
236 2944 (2016).
- 237 26. Matrà, L. *et al.* Detection of exocometary co within the 440 myr-old fomalhaut belt: A similar CO+CO2
238 ice abundance in exocometes and solar system comets. *arXiv* **842**, 9 (2017).
- 239 27. Kral, Q., Matrà, L., Wyatt, M. C. & Kennedy, G. M. Predictions for the secondary CO, C and O gas
240 content of debris discs from the destruction of volatile-rich planetesimals. *\mnras* **469**, 521–550 (2017).
- 241 28. Zuckerman, B. & Song, I. A 40Myr old gaseous circumstellar disk at 49 CETI: Massive CO-rich comet
242 clouds at young a-type stars. *Astrophys. J.* **758**, 77 (2012).
- 243 29. Prialnik, D. & Rosenberg, E. D. Can ice survive in main-belt comets? Long-term evolution models of
244 comet 133P/Elst-Pizarro. *Mon. Not. R. Astron. Soc. Lett.* **399**, L79–L83 (2009).

- 245 30. Snodgrass, C. *et al.* The Main Belt Comets and ice in the Solar System. *aapr* **25**, 5 (2017).
246 31. Marino, S. *et al.* ALMA observations of the η Corvi debris disc: inward scattering of
247 CO-rich exocomets by a chain of 3-30 M_{\oplus} planets? *mrras* **465**, 2595–2615
248 (2017).
249 32. Benz, W., Anic, A., Horner, J. & Whitby, J. ~A. The Origin of Mercury. *ssr* **132**, 189–202 (2007).
250 33. Chau, A., Reinhardt, C., Helled, R. & Stadel, J. Forming Mercury by Giant Impacts. *apj* **865**, 35
251 (2018).
252 34. Canup, R. M. Simulations of a late lunar-forming impact. *icarus* **168**, 433–456 (2004).
253 35. Canup, R. M. Forming a Moon with an Earth-like Composition via a Giant Impact. *Science (80-.)*. **338**,
254 1052 (2012).
255 36. Mastrobuono-Battisti, A., Perets, H. B. & Raymond, S. N. A primordial origin for the compositional
256 similarity between the Earth and the Moon. *nat* **520**, 212–215 (2015).
257 37. Marinova, M. M., Aharonson, O. & Asphaug, E. Mega-impact formation of the Mars hemispheric
258 dichotomy. *nat* **453**, 1216–1219 (2008).
259 38. Nimmo, F., Hart, S. ~D., Korycansky, D. ~G. & Agnor, C. ~B. Implications of an impact origin for the
260 martian hemispheric dichotomy. *nat* **453**, 1220–1223 (2008).
261 39. Davies, J. H. Did a mega-collision dry Venus’ interior? *Earth Planet. Sci. Lett.* **268**, 376–383 (2008).
262 40. Wyatt, M. C. & Jackson, A. P. Insights into Planet Formation from Debris Disks: II. Giant Impacts in
263 Extrasolar Planetary Systems. *Space Sci. Rev.* **205**, 231–265 (2016).
264 41. Heays, A. N., Bosman, A. D. & van Dishoeck, E. F. Photodissociation and photoionisation of atoms and
265 molecules of astrophysical interest. *arXiv* **602**, (2017).
266 42. Schlichting, H. E. & Mukhopadhyay, S. Atmosphere Impact Losses. *Space Sci. Rev.* **214**, 34 (2018).
267 43. Kegerreis, J. ~A. *et al.* Atmospheric Erosion by Giant Impacts onto Terrestrial Planets: A Scaling Law
268 for any Speed, Angle, Mass, and Density. *apjl* **901**, L31 (2020).
269 44. Lammer, H. *et al.* Origin and evolution of the atmospheres of early Venus, Earth and Mars. *Astron.*
270 *Astrophys. Rev.* **26**, 2 (2018).
271 45. Biersteker, J. B. & Schlichting, H. E. Atmospheric mass-loss due to giant impacts: The importance of
272 the thermal component for hydrogen-helium envelopes. *Mon. Not. R. Astron. Soc.* **485**, 4454–4463
273 (2019).
274

275 **Methods**

276

277 **ALMA observations.** We analyzed archival data from the ALMA telescope taken during Cycle 1 in band 6
278 (project code 2012.1.00437.S). The observations were performed with the 12-m array in a compact antenna
279 configuration. The on-source time was 76 minutes. The spectral setup included four spectral windows, of which
280 three were set up in time division mode for continuum observations and centered at 213, 215, and 228 GHz. One
281 window was set in frequency division mode (with high spectral resolution of 488.29 kHz) to target the ^{12}CO J=2-
282 1 line (rest frequency 230.538 GHz). We calibrated the visibility data using scripts provided by the ALMA
283 observatory. The CASA softwareⁱⁱ (version 5.6.1) was used for visibility imaging. For both the continuum and
284 CO line emission, we removed data from antennas 7, 19, and 25. These data were taken in a hybrid configuration,
285 with the three flagged antennas far from the compact group of antennas; removing these data significantly
286 improves the imaging.

287 The CLEAN algorithm⁴⁶ was used to image both the continuum and CO line emission through the CASA
288 *clean* task. To achieve maximum sensitivity, we used natural weighting for both datasets, resulting in a
289 synthesized beam size of $1.16'' \times 0.75''$, corresponding to 32.9×21.3 au at the system distance (28.5 pc) and
290 position angle of 81° . Before line imaging, we subtracted the continuum (measured in line-free regions of the
291 spectrum) in visibility space using the CASA *uvcontsub* task. We then imaged the CO to produce a cube with
292 frequencies within ± 25 MHz of the rest frequency, corresponding to velocities within ± 30 km/s of the radial
293 velocity of the star. The data were imaged at the native spectral resolution (twice the original channel width) of
294 488.29 kHz. To obtain the CO moment-0 map, shown in Figure 1, we integrated along the velocity axis between
295 ± 15 km/s of the stellar velocity.

296 The emission is spatially unresolved in both the continuum and CO images, which have RMS noise levels
297 of $0.029 \text{ mJy beam}^{-1}$ and $26 \text{ mJy km s}^{-1} \text{ beam}^{-1}$, respectively. This yields a peak detection at a SNR per beam of 4
298 and 6 for the continuum and CO J=2-1 spectrally integrated emission, and total fluxes of $0.12 \pm 0.03 \text{ mJy}$ and 170
299 $\pm 30 \text{ mJy km/s}$, respectively. Note that the flux calibration is expected to be accurate within 10%; this uncertainty
300 was added in quadrature to obtain the quoted errorsⁱⁱⁱ. Both the CO gas and continuum dust emission centroids are
301 consistent with the *Gaia* proper-motion corrected position of the system^{7,8}. To extract a 1D spectrum from the
302 data cube, we integrate within a circular mask of radius $2.5\sigma_{\text{beam}}$ (with σ_{beam} being the standard deviation of the
303 2D Gaussian beam, averaged between the major and minor axis).

304

305 **Millimetre dust mass.** To calculate the dust mass, we assume the dust grains act as blackbodies and emit
306 according to their Planck function at a temperature of 169 K. Assuming the dust is optically thin, the total dust
307 mass can be calculated from the observed emission ($F_{\nu} = 0.12 \pm 0.03$ mJy), when accounting for the stellar
308 contribution. This contribution is estimated to be 0.035 mJy at 230 GHz from our best fit PHOENIX stellar model
309 fitted to optical and near-IR photometry (see ‘Optically thin CO mass calculation’ section below). PHOENIX
310 models have been shown to be a good fit to mm-wavelength photometry of Sirius A⁴⁷ which has a similar spectral
311 type to HD 172555. Subtracting this stellar contribution to the detected mm emission yields a contribution due to
312 dust of 85 ± 30 μ Jy. The dust grain opacity is assumed to be $10 \text{ cm}^2 \text{ g}^{-1}$ at 1000 GHz and scaled to the frequency
313 of the observation with an opacity power law index of $\beta = 1$ ⁴⁸. These assumptions yield a dust mass of (1.8 ± 0.6)
314 $\times 10^{-4} M_{\oplus}$.

315

316 **Optically thin CO ring modelling.** To model the velocity spectrum expected from a circular orbiting ring or disk
317 of material, we calculate Keplerian velocities assuming a stellar mass of $1.76 M_{\odot}$ ⁶. 2D orbital velocity vectors are
318 calculated for a radial and azimuthal grid, assuming a vertically thin ring/disk of gas that has radially and
319 azimuthally uniform surface density between an inner and outer boundary. They are transformed to the sky plane
320 using the ring/disk inclination to obtain radial velocities along the line-of-sight. These velocities in the reference
321 frame of the star are then added to the radial velocity of the star in the barycentric frame (left as a free parameter)
322 to obtain barycentric velocities as observed by ALMA. A histogram of these velocities, with the same binning as
323 the observed data, serves as a model spectrum. We normalize the unitless spectrum such that the integral of the
324 spectrum is equal to the integrated flux of the line, a free parameter in the fit. This spectrum is then convolved
325 with a Gaussian of FWHM equal to twice the channel width to reproduce the spectral response of the instrument
326 due to Hanning smoothing^{iv}. In addition to these parameters, the model fits the inclination, radial location of the
327 midpoint, and width of the ring/disk.

328

329 A Markov Chain Monte Carlo (MCMC) approach was used to determine the best fit to the data. We used
330 the Python package *emcee*⁴⁹. The uncertainty in each velocity bin was assumed to be equal to the RMS measured
331 in the region of the spectrum outside the detected emission. Flat priors were applied for the radial location, width,
332 integrated line flux, and stellar velocity. A Gaussian prior was applied to the inclination, assuming the gas shares
333 the same inclination as the dust disk, as determined from previous resolved imaging¹². We carried out an additional
run where a flat prior was applied to the inclination, to confirm the assumption of shared inclination. Extended

334 Data Fig. 1 shows the posterior probability distributions of the parameters obtained from our MCMC runs,
335 whereas Extended Data Table 1 indicates the best-fit values, obtained as the $50^{\text{th}} \pm 34^{\text{th}}$ percentiles of the posterior
336 distributions of each parameter, marginalized over all other parameters. Best fit values from both runs assuming
337 a Gaussian or flat prior on the inclination are included.

338

339 **Optically thin CO mass calculation.** To derive a CO mass from the best-fit spectrally-integrated line flux, we
340 begin by assuming that the line is optically thin and considering the excitation conditions the gas may be subject
341 to, which affect this conversion. We follow an existing framework²⁴, which considers that the energy levels of a
342 CO molecule may be populated by collisions with other species (or by one dominant species, the main collisional
343 partner), or by absorption and emission of radiation, giving rise to two limiting regimes, a radiation-dominated
344 regime (at low gas densities), and a collision-dominated regime (local thermodynamic equilibrium, LTE, at high
345 gas densities). The choice of density of collisional partners (in our case, electrons) does not affect the level
346 populations in these two limiting regimes, and therefore the range of CO masses derived.

347 To account for the full range of excitation conditions, we therefore use a non-LTE code²⁴ to solve the statistical
348 equilibrium equations and calculate the level populations. This includes the effect of fluorescence induced by
349 stellar UV and IR radiation as seen by a CO molecule at 7.5 au from the central star⁵⁰. For the star, we adopt a
350 PHOENIX⁵¹ model spectrum fitted to multiband optical and near-IR photometry using the MultiNest code⁵², as
351 described in previous works^{53,54}. This yields a best-fit stellar effective temperature of $T_{\text{eff}} = 7840 \pm 30$ K, and
352 luminosity of $L_{\star} = 7.7 \pm 0.1 L_{\odot}$. The non-LTE calculation yields a formal range of possible CO masses between
353 $(0.45 - 1.21) \times 10^{-5} M_{\oplus}$ for kinetic temperatures between 100 and 250 K, encompassing the blackbody
354 temperature of 169 K at 7.5 au.

355

356 **3D radiative transfer modelling.** We use the RADMC-3D^{11,v} radiative transfer code to check the impact of
357 optical depth in more detail. We use the same ring geometry as obtained from optically thin fitting (Extended Data
358 Table 1, Gaussian prior). We vary the input CO mass and kinetic temperature over a 2D grid (Figure 2b), and
359 connect the latter to the vertical aspect ratio by assuming a vertically isothermal gas disk with a mean molecular
360 weight of 14 (i.e. the gas mass is dominated by atomic C and O, as expected in a second generation scenario). In
361 order to sample the ring well spatially and spectrally, we create cubes of J=2-1 emission with a pixel size of 6 mas

¹¹ <http://www.ita.uni-heidelberg.de/~dullemond/software/radmc-3d/>

362 (corresponding to a physical scale of 0.18 au), and the same native channel width as our data. We then spectrally
363 convolve with a Gaussian to reproduce the spectral response of the instrument and extract a 1D model spectrum
364 by spatially integrating the model emission. We then compared this model spectrum to the data (as shown in
365 Figure 2a) and calculated a χ^2 for every mass and temperature in our grid, to obtain a χ^2 map (Figure 2b).

366

367 **CO survival lifetime against photodissociation.** The observed CO gas in the circumstellar environment around
368 HD 172555 will be subject to photodissociation from the stellar and interstellar UV field. The photodissociation
369 rate in s^{-1} of a molecule in a radiation field $I(\lambda)$ is $k = \int \sigma(\lambda)I(\lambda)d\lambda$, where $\sigma(\lambda)$ is the photodissociation cross
370 section in cm^2 . We use the CO photodissociation cross sections from the Leiden database^{41,vi}. We adopt the stellar
371 spectrum from the optically thin mass section above, scaled to the center of the gas ring (7.5 au) to obtain the
372 stellar radiation field. We find that the star dominates over the interstellar radiation field, and that the CO
373 photodissociation timescale ($1/k$) at the ring's radial location is approximately a day. The shielding effects are
374 estimated using pre-computed shielding constants⁴¹; we interpolate the constants for stars of 4000 and 10000 K
375 to a stellar temperature of 8000 K, closest to HD172555's effective temperature. The CO column density is
376 calculated from the center of the ring along the line of sight to the star, using our best-fit uniform ring model
377 parameters. To find the H_2 and C column densities that provide sufficient shielding, we interpolate the shielding
378 constants along the column density axis and find the column density required.

379

380 **Delivery from an outer belt.**

381 Replenishment requirement We consider a scenario where the dust grains and CO gas are produced from
382 sublimation-driven release by Solar System -like comets entering the inner region of the HD172555 system. This
383 requires replenishment of the observed total dust mass (in grains up to cm in size) on timescales comparable to
384 their removal (assuming steady state). We assume their removal is dominated by collisions, setting up a cascade
385 down to the smallest grains (of size $\sim 3.5 \mu\text{m}$ for a grain density of 2700 kg m^{-3}) that are then removed by radiation
386 pressure from the central star, to derive a mass loss rate of $2.2 \times 10^{-2} M_{\oplus} \text{ Myr}^{-1}$ (using Eq. 21 in ²⁶). We neglect
387 the effect of gas drag, assuming that the larger, cm grains are unaffected.

388 We use the results of thermochemical modelling⁵⁵ calibrated on Solar System comets to estimate the mass loss
389 rate per unit surface area of an exocomet at 7.5 au around a $7.7 L_{\odot}$ to be $5.6 \times 10^{-6} \text{ kg m}^{-2} \text{ s}^{-1}$ of dust in grains up
390 to cm in size. Dividing by an assumed bulk density of 560 kg m^{-3} , and assuming a 1:1 dust/ice ratio, this

391 corresponds to an erosion rate of 0.62 m yr^{-1} . Therefore, a comet with a 10 km radius will be emitting dust at a
392 rate of 7040 kg/s ($3.72 \times 10^{-8} M_{\oplus} \text{ Myr}^{-1}$), and will survive (if continuously sublimating at this rate) for $\sim 16 \text{ kyr}$.

393

394 *High eccentricity exocomet population* In the first case, we assume exocomets arise from a yet undetected belt at
395 100 au (a typical location of cold exocometary belts around A stars⁵⁶) and approach the inner regions on eccentric
396 orbits. The velocity distribution from the observed CO emission implies line-of-sight velocities for the gas of
397 $\sim 14.5 \text{ km/s}$, corresponding to 7.5 au for circular orbits around HD172555. However, these velocities will be
398 achieved at larger radii for comets with non-zero eccentricities, random pericentre directions, and orbiting in the
399 same plane as HD172555's inner system. The pericentre distance corresponding to pericentre velocities of ~ 14.5
400 km/s will increase with the apocenter (and therefore the eccentricity) of the orbits; for an apocenter of 100 au, we
401 derive a pericentre distance of 13.2 au. Therefore, we expect gas released from exocomets on these orbits to be
402 located at and beyond $\sim 13.2 \text{ au}$ from the central star. For comparison, this is 80% larger than the radial location
403 derived for circular orbits (7.5 au). However, eccentric exocomets with the observed velocities would produce a
404 CO ring with diameter $\sim 26 \text{ au}$ ($0.9''$), which is comparable to the resolution element of our observations, implying
405 the ring would have been marginally resolved, which is not the case. Additionally, scattered light observations
406 strongly constrain dust emission to $< 0.9''$ (3σ) diameter, with a sharp outer edge. The fact that the expected radius
407 of a CO ring would significantly exceed the observed value makes the eccentric exocomet scenario inconsistent
408 with the available observations. Note that reasonably changing the apocenter location, and therefore the radius of
409 the hypothetical cold belt where the exocomets originate, does not alter our conclusions significantly. For
410 example, assuming an outer belt location of 20 instead of 100 au implies exocomet pericenters at 10 au. This
411 would produce CO emission with a minimum expected diameter of 20 au ($0.7''$) and extending much beyond it,
412 which likely would have been spatially resolved in the ALMA data.

413

414 *Low eccentricity exocomet population* In the second case, we assume exocomets are being continuously scattered
415 inward from an outer belt by a chain of low mass planets, undergoing multiple scatterings and producing a low
416 eccentricity comet population at $\sim 7.5 \text{ au}$. We here assume circular orbits for simplicity. The dust observed requires
417 replenishment at a rate of $2.2 \times 10^{-2} M_{\oplus} \text{ Myr}^{-1}$. Assuming exocomets of 10 km in size with an exocometary dust
418 release rate of $3.72 \times 10^{-8} M_{\oplus} \text{ Myr}^{-1}$, 5.9×10^5 exocomets are required to be sublimating at around $\sim 7.5 \text{ au}$ at any
419 point in time. For a bulk density of 560 kg m^{-3} , this corresponds to $2.3 \times 10^{-4} M_{\oplus}$ in 10 km exocomets. While
420 sublimating at this rate, such an exocomet would survive for $\sim 16 \text{ kyr}$, so comets would need to be resupplied by

421 inward scattering to the inner planetary system at a rate of $1.4 \times 10^{-8} M_{\oplus} \text{ yr}^{-1}$. Inward scattering is an inefficient
422 process; simulations maximising inward scattering by chains of low mass planets indicate that only a few % of
423 comets encountering an outermost planets make it into the inner regions, as the vast majority are ejected⁵⁷.
424 Therefore, higher supply rates of order $\sim 10^{-6} M_{\oplus} \text{ yr}^{-1}$ from a putative outer belt are likely needed, which would
425 imply that a currently undetected outer belt would have resupplied $23 M_{\oplus}$ in 10 km exocomets into the inner
426 regions over the 23 Myr age of the system.

427 We can compare this to the upper limit on the presence of an outer belt at 100 au from our ALMA data. Assuming
428 blackbody temperatures, and the same dust opacity as used for dust in the inner regions, we derive an upper limit
429 of $< 1.8 \times 10^{-3} M_{\oplus} (3\sigma)$ on the mass of solids of sizes up to cm sizes. Extrapolating from cm sized grains up to 10
430 km exocomets (assuming a size distribution with a constant power law slope of -3.5) we obtain an upper limit on
431 the total mass in 10 km sized exocomets of $< 1.8 M_{\oplus} (3\sigma)$. Therefore, the *current* mass of the outer belt would be
432 at least a factor ~ 10 smaller than the mass that has been removed from the belt over its lifetime, which is by itself
433 not impossible.

434 However, it is likely that exocomets reaching their inner regions would retain some eccentricity, which would
435 prolong their survival (lower sublimation rates), but also potentially make the gas velocity distribution inconsistent
436 with the observations. In addition to that, the narrow CO radial distribution is in tension with production rates of
437 CO as a function of heliocentric distance in sublimating Solar System comets⁵⁸, which show no clear enhancement
438 in production rates at radii whose thermal conditions are comparable to HD172555's. While inward scattered,
439 sublimating exocomets could produce a steeper than collisional size distribution of grains, down to sizes smaller
440 than the radiation pressure blow-out limit, they would not be able to reproduce the peculiar dust mineralogy
441 indicative of energetic processing typical of hypervelocity impacts, unless exocometary impacts in the inner
442 regions contribute, and/or are the source of the dust and gas observed. In conclusion, sublimating exocomets
443 could be replenished in the inner system at high enough rates to explain the observed dust emission, but are
444 unlikely to explain the relatively narrow distribution of CO, and the dust mineralogy observed around HD172555.

445

446

447 **In situ giant impact constraints from axisymmetry and width of debris.** Observations of both CO and dust^{11,12}
448 are consistent with the CO and dust distribution being axisymmetric. Because of this, the time since impact must
449 be at least the symmetrization timescale, which is on the order of a few tens of thousands of orbits⁴⁰ (~ 0.2 Myr at
450 7.5 au). Constraints on the planet mass can be derived from the width of the debris, as a proxy for the velocity

451 dispersion of released material. The width, dr , is given by $dr = 2re_p$, where e_p is the proper eccentricity of the
452 orbiting debris⁵⁹. This eccentricity is related to the velocity dispersion, σ_v , through $\sigma_v \sim \sqrt{1.5}e_p v_k$, where v_k is
453 the keplerian velocity at the given semimajor axis. We assume the velocity dispersion is related to the escape
454 velocity of the colliding bodies⁴⁰ by $\sigma_v \sim 0.46v_{esc} \sim 0.46 \sqrt{\frac{2GM_p}{R_p}}$. Thus, for an observed debris width dr , a planet
455 of mass $M_p \sim 103 \frac{M_*^{3/2}}{\rho_p^{1/2}} \left(\frac{dr}{r^{3/2}}\right)^3$ in M_\oplus is expected, where ρ_p is the planet's bulk density in g cm^{-3} , M_* is the stellar
456 mass in M_\odot , and both r and dr are in au. If the planetary bodies colliding have rocky, Earth-like compositions,
457 they will have bulk densities of $\sim 5.5 \text{ g cm}^{-3}$. We assume that the solid debris is confined to the same radial width
458 as the dust width derived from mid-IR Q band imaging¹¹, which finds $dr_{dust}/r \sim 1.2$. These assumptions yield a
459 planetary mass on the order of $\sim 8 M_\oplus$. We note that mid-IR imaging is sensitive to small grains whose width
460 might have been broadened due to radiation pressure from the central star; if radiation pressure inflated the width
461 compared to that expected from the velocity dispersion, the planetary mass involved would be reduced. If instead
462 the bulk planetary density is lower, the mass of planet involved in the collision would be larger.

463

464 **Constraints from debris survival.** Progenitor mass constraints must also be considered in the context of debris
465 survival; the observed debris must survive encounters with a leftover planet in the time since impact. We
466 conservatively assume that the mass of the largest product of the impact is on the order of the mass of the impact
467 progenitors, and consider the outcome of encounters between debris and a surviving planet⁶⁰. Given an assumed
468 planetary density similar to that of the Earth, and a semimajor axis of 7.5 au, we first note that for a leftover planet
469 with mass below $\sim 1.8 M_\oplus$, the predominant (eventual) outcome of an encounter will be accretion, whereas for
470 masses above that threshold, the predominant (eventual) outcome will be ejection. However, timescales of
471 accretion and ejection play a role in debris survival. These timescales must be at least as long as the
472 symmetrization timescale (0.2 Myr) to ensure debris produced in an impact could be seen in the symmetrical
473 structure observed today. For progenitor masses in the range derived from the debris width constraints above, the
474 reaccretion and ejection timescales are much longer than the symmetrization timescale. Therefore, giant impact
475 debris at 7.5 au is expected to survive encounters with leftover planets with masses on the order of $8 M_\oplus$, as large
476 as those of the progenitors, on a timescale longer than the symmetrization timescale.

477

- 478
479 46. HÖGBOM, J. & CORNWELL, T. APERTURE SYNTHESIS WITH A NON-REGULAR
480 DISTRIBUTION OF INTERFEROMETER BASELINES. *Commentary. Astron. Astrophys. (Berlin.*
481 *Print)* **500**, 55–66 (2009).
482 47. White, J. A. *et al.* The MESAS Project: Long-wavelength Follow-up Observations of Sirius A. *apj* **875**,
483 55 (2019).
484 48. Beckwith, S. V. W., Sargent, A. I., Chini, R. S. & Guesten, R. A survey for circumstellar disks around
485 young stellar objects. *Astron. J.* **99**, 924 (1990).
486 49. Foreman-Mackey, D., Hogg, D. W., Lang, D. & Goodman, J. emcee: The MCMC Hammer. 1–15
487 (2012) doi:10.1086/670067.
488 50. Matrà, L. *et al.* Molecular reconnaissance of the β pictoris gas disk with the SMA: A low
489 HCN/(CO+CO₂) outgassing ratio and predictions for future surveys. *arXiv* **853**, 147 (2018).
490 51. Husser, T. O. *et al.* A new extensive library of PHOENIX stellar atmospheres and synthetic spectra.
491 *Astron. Astrophys.* **553**, A6 (2013).
492 52. Feroz, F., Hobson, M. P. & Bridges, M. MultiNest: An efficient and robust Bayesian inference tool for
493 cosmology and particle physics. *Mon. Not. R. Astron. Soc.* **398**, 1601–1614 (2009).
494 53. Sepulveda, A. G. *et al.* The REASONS Survey: Resolved millimeter observations of a large debris disk
495 around the nearby F star HD 170773. *arXiv* **881**, 84 (2019).
496 54. Yelverton, B., Kennedy, G. M., Su, K. Y. L. & Wyatt, M. C. A statistically significant lack of debris
497 discs in medium separation binary systems. *Mon. Not. R. Astron. Soc.* **488**, 3588–3606 (2019).
498 55. Marboeuf, U., Bonsor, A. & Augereau, J. C. Extrasolar comets: The origin of dust in exozodiacal disks?
499 *Planet. Space Sci.* **133**, 47–62 (2016).
500 56. Matrà, L. *et al.* An empirical planetesimal belt radius - stellar luminosity relation. *arXiv* **859**, 72 (2018).
501 57. Marino, S., Bonsor, A., Wyatt, M. C. & Kral, Q. Scattering of exocomets by a planet chain: Exozodi
502 levels and the delivery of cometary material to inner planets. *Mon. Not. R. Astron. Soc.* **479**, 1651–1671
503 (2018).
504 58. Biver, N. *et al.* The 1995-2002 long-term monitoring of comet C/1995 O1 (Hale-Bopp) at radio
505 wavelength. *Earth, Moon Planets* **90**, 5–14 (2002).
506 59. Wyatt, M. C. *et al.* How Observations of Circumstellar Disk Asymmetries Can Reveal Hidden Planets:
507 Pericenter Glow and Its Application to the HR 4796 Disk. *Astrophys. J.* **527**, 918–944 (1999).
508 60. Wyatt, M. C., Bonsor, A., Jackson, A. P., Marino, S. & Shannon, A. How to design a planetary system
509 for different scattering outcomes: Giant impact sweet spot, maximizing exocomets, scattered discs.
510 *Mon. Not. R. Astron. Soc.* **464**, 3385–3407 (2017).

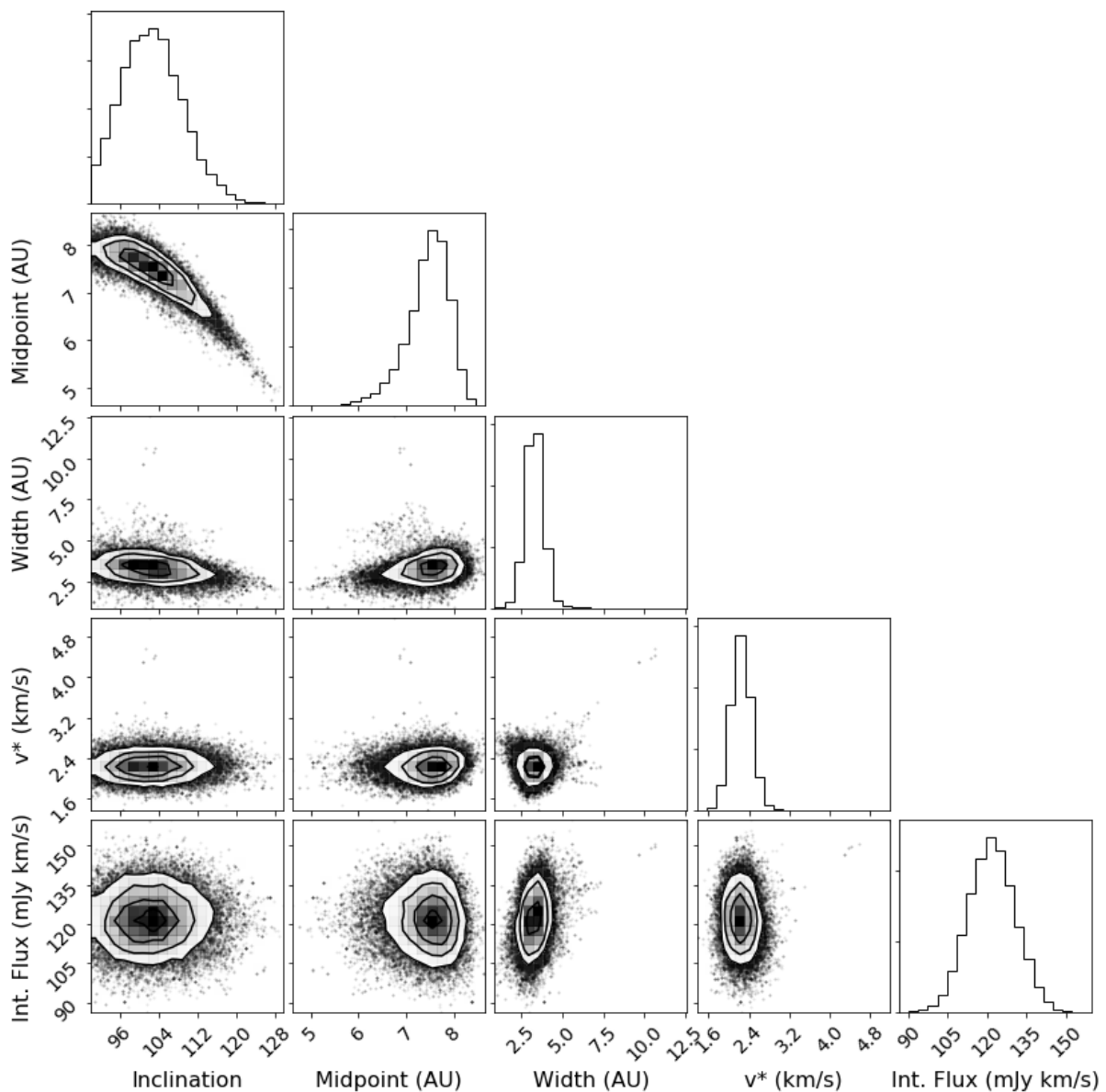
511
512

513 **Acknowledgements.** We are grateful to John Biersteker for discussions on the liberation of atmospheres in the
514 aftermath of giant impacts. This paper makes use of ALMA data ADS/JAO.ALMA#2012.1.00437.S. ALMA is
515 a partnership of ESO (representing its member states), NSF (USA) and NINS (Japan), together with NRC
516 (Canada), NSC and ASIAA (Taiwan), and KASI (Republic of Korea), in cooperation with the Republic of Chile.
517 The Joint ALMA Observatory is operated by ESO, AUI/NRAO and NAOJ. KIÖ acknowledges support from the
518 Simons Foundation (SCOL #321183). GMK is supported by the Royal Society as a Royal Society University
519 Research Fellow.

520 **Author Contributions** T.S. led the optically thin modelling and discussion. L.M. led the radiative transfer
521 modelling. Both authors were involved in data reduction, processing, and writing of the manuscript. All authors
522 contributed to discussions of the results and commented on the manuscript.

523 **Competing interests declaration** The authors declare no competing interests.

524 **Data Availability** The ALMA program number for the presented data is 2012.1.00437.S and data can be found
 525 in the online ALMA archive. The cleaned .fits files are available upon request.
 526 **Code Availability** RADMC-3D (<https://github.com/dullemond/radmc3d-2.0>) and *emcee*
 527 (<https://emcee.readthedocs.io/en/stable/>) are available online. Custom code, including the ring model and non-
 528 LTE code, is available online (https://github.com/tmschneiderman/hd172555_CO_2021).
 529 **Additional Information** Correspondence and requests for materials should be addressed to T.S.
 530 (tajana@mit.edu).



531

532 **Extended Figure 1.** Posterior probability distributions for the model parameters obtained from the *emcee* fitting
 533 process. All parameters are well constrained, with best fit values listed in Extended Data Table 1. This model

534 was fitted to spectral data retaining original channel widths, assumed a Gaussian prior on the inclination, and
 535 assumed a stellar mass of $1.76 M_{\odot}$
 536

Best fit parameters		
	Gaussian	Flat
Inclination ($^{\circ}$)	102 +6.0 -6.5	107 +12.1 -17.6
Midpoint (au)	7.4 +0.5 ^w -0.4	7.4 +1.8 -0.6
Width (au)	3.4±0.5	3.1 +0.9 -0.7
V_* (km/s)	2.3±0.2	2.3±0.2
Int. Flux (mJy km/s)	122 +8.9 -9.0	122 +8.5 -8.8

537
 538 **Extended Data Table 1:** Best fit values (50±34 percentile) to the optically thin model of gas emission. Left
 539 column indicates values derived from the MCMC run where a Gaussian prior was applied to the inclination. Right
 540 column indicates values derived from the MCMC run where flat priors were applied to all model parameters.

ⁱ The literature¹¹ values for the dust location in au have been corrected to account for the new GAIA distance to the star compared to previous Hipparcos distance.

ⁱⁱ <https://casa.nrao.edu/casadocs/casa-5.6.0>

ⁱⁱⁱ <https://almascience.nrao.edu/documents-and-tools/cycle-1/alma-ot-reference-manual>

^{iv} https://safe.nrao.edu/wiki/pub/Main/ALMAWindowFunctions/Note_on_Spectral_Response.pdf

^v <http://www.ita.uni-heidelberg.de/~dullemond/software/radmc-3d/>

^{vi} https://home.strw.leidenuniv.nl/~ewine/photo/display_co_42983b05e2f2cc22822e30beb7bdd668.html